Impact of EMIC-wave driven electron precipitation on the radiation belts and the atmosphere

A. T. Hendry[1,2], A. Seppälä[1], C. J. Rodger[1], M. A. Clilverd[3]

[1]University of Otago, Dunedin, New Zealand
[2]Department of Space Physics, Institute of Atmospheric Physics, Prague, Czechia
[3]British Antarctic Survey (NERC), Cambridge, UK

Key Points:

- Observations of sub-MeV EMIC-driven electron precipitation do not contradict observed relativistic trapped flux dropout responses.
- EMIC-driven electron precipitation can cause significant increases in mesopheric HO_x and NO_x, leading to decreases in mesospheric ozone.
- EMIC-driven EEP is not appropriately accounted for by common geomagnetic activity proxies used in climate modelling.

Corresponding author: Aaron T. Hendry, aaron.hendry@otago.ac.nz

Abstract

In recent years there has been a growing body of direct experimental evidence demonstrating electromagnetic ion cyclotron (EMIC) waves driving energetic electron precipitation (EEP) at unexpectedly low, sub-MeV energies — as low as only a few hundred keV. EMIC wave driven scattering at these energies has important ramifications for our understanding of not only radiation belt electron dynamics, but also the importance of EMIC-driven EEP to the chemical balance of the Earth's atmosphere. In this study, we use three experimentally derived EMIC-driven EEP flux spectra to investigate the impact of this precipitation on trapped radiation belt fluxes. In doing so, we resolve an apparent contradiction with earlier results derived from trapped electron flux populations that suggested EMIC waves only caused significant scattering at ultra-relativistic energies. We show that strong sub-MeV EEP measurements are not necessarily mutually exclusive with a strongly relativistic-only trapped flux response, as the sub-MEV peak precipitation is comparatively much smaller than the trapped population at those energies. Using a further six EEP spectra, we also demonstrate that EMIC-driven EEP can generate significant ionisation of the Earth's atmosphere above 40km, leading to the loss of mesospheric ozone. We find poor correlation between EMIC-driven EEP fluxes and geomagnetic activity proxies, such that EMIC-driven EEP is likely to be poorly specified in the forcing factors of modern coupled-climate models.

1 Introduction

The Earth's radiation belts are complex and dynamic, driven by ever-changing particle acceleration, loss, and transport processes. In recent years, there has been a heightened interest in radiation belt loss processes and the impact these losses have on the belts and the Earth's atmosphere (e.g., Friedel et al., 2002; R. Millan & Thorne, 2007; Newnham et al., 2018; van de Kamp et al., 2018). Energetic electron loss to the atmosphere in particular has been recognised as a potential driver of regional scale variability in surface air temperatures (Seppälä et al., 2009), and has been highlighted as a necessary component of comprehensive climate models (Matthes et al., 2017). Clearly, understanding the effects of different electron loss drivers is essential to quantifying the role that electron precipitation plays in affecting the broader climate.

One of the primary drivers of particle loss from the radiation belts is the interaction between these particles and magnetospheric plasma waves (e.g., Thorne, 2010). One such wave-particle interaction that has been the subject of considerable academic debate in recent years occurs between radiation belt electrons and electromagnetic ion cyclotron (EMIC) waves. EMIC waves are coherent, typically circularly polarised Pc1-2 (0.1–5 Hz) waves generated near the geomagnetic equator, often during periods of heightened geomagnetic activity (e.g., Clausen et al., 2011). Despite over half a century of study, however, there are still many key questions regarding EMIC waves and their interactions with the radiation belt that remain unanswered, including the energy limits of the EMIC-electron interaction, the effects of this interaction on radiation belt electron populations, and the impacts of the resulting electron precipitation on the upper atmosphere.

There has been significant debate regarding the first of these questions. Despite early experimental work hinting that the minimum energy of EMIC-electron interactions could be as low as hundreds of keV (e.g., Gendrin et al., 1967; Jacobs, 1970), later theoretical results using in-situ satellite wave observations suggested that in all but the most extreme cases, electron precipitation could be expected only at energies $> 1 - 2$ MeV (e.g., Meredith et al., 2003). In recent years, however, there has been a growing body of experimental evidence from many different instruments to suggest that EMIC-driven energetic electron precipitation (EEP) might occur readily at energies below 1 MeV (e.g., R. M. Millan et al., 2007; Woodger et al., 2015; Clilverd et al., 2015; Rodger et al., 2015; Hendry et al., 2017, 2019). One of the most important of these results was the broad statistical survey of POES MEPED data carried out by Hendry et al. (2017), who showed that not only were these sub-MeV EMIC-driven EEP events possible, but that they appeared to be the dominant form of EMIC-driven EEP seen in the POES data. The reason for the disjunction between the experimental data and the theoretical predictions is still unclear; suggested solutions have included non-linear (e.g., Omura & Zhao, 2013; Kubota & Omura, 2017; Hendry et al., 2019) and non-resonant (Chen et al., 2016) interactions, as well as interactions between simultaneous He+ and H+ band waves (Denton et al., 2019), although to date a consensus has yet to be reached.

Theoretical considerations aside, the existence of EMIC-driven EEP at these relatively low energies raises some important questions: Why have other statistical investigations of EMIC waves not seen similar sub-MeV EEP (e.g., Usanova et al., 2014)? Given that these events are occurring, what is the impact of this EEP on trapped electron fluxes? What is the effect on the upper atmosphere? The latter two of these questions are of particular interest; if EMIC waves are able to access the sub-relativistic (i.e., hundreds of keV) population of the radiation belt electron population and drive meaningful levels of precipitation at these energies, they may not only be able to deplete the radiation belts but are also likely cause significant changes to the Earth's atmospheric chemistry.

Particle precipitation is a well known source of Odd nitrogen (NO_x = NO + NO_2) and Odd hydrogen (HO_x = OH + HO_2) gases in the polar mesosphere and stratosphere (between altitudes of ∼30-90 km) (Seppälä et al., 2014). These gases act as catalysts in ozone loss reaction cycles, resulting in rapid in situ ozone loss immediately following EEP events (M. E. Andersson et al., 2014). Modelling of different precipitation events and drivers has suggested that EEP is the cause of significant impacts to atmospheric chemistry (e.g., Rodger et al., 2007; Seppälä et al., 2018). EEP is also known to drive a delayed loss process — the so called *EEP-indirect* effect (Randall et al., 2006). This process occurs months after the initial precipitation, following transport of the EEP-NO_x down (from the typical EEP altitudes near 70-80 km) to the stratosphere below 50 km (Gordon, Seppälä, & Tamminen, 2020).

Once in the stratosphere this EEP-NO_x can contribute to long term ozone variability in complex ways: recent observational evidence has shown that in addition to directly causing ozone loss, EEP-NO_x can also cause indirect increases in ozone at the main ozone layer altitudes by binding harmful, ozone hole causing halogen compounds, thus preventing them from contributing to springtime polar ozone loss (Gordon, Seppälä, Funke, et al., 2020). The ability to correctly estimate and model atmospheric ozone levels is critical for climate simulations as, for example, ozone provides a critical source for heating and cooling in the atmosphere linking it to dynamical patterns and regional climate variability (Matthes et al., 2017). Due to the many unknowns surrounding EMIC-driven EEP, it is unclear how well EMIC precipitation is accounted for by the current EEP proxies used in atmospheric and climate modelling (Matthes et al., 2017; van de Kamp et al., 2018).

In the next section, we discuss the instrumentation used in this study, including a detailed discussion of the database of EMIC-driven EEP events in Section 2.1. Following this, we investigate the impact of EMIC-driven EEP on the radiation belts by simulating the response of a model trapped flux population to EMIC-driven scattering, using experimental observations of EMIC-driven EEP to calculate the expected flux dropout (Section 3). We then use additional observations of EMIC-driven EEP to drive an atmospheric neutral and ion chemistry model, allowing us to investigate the impact of EMIC-driven electron scattering on the Earth's atmosphere (Section 4). We study the seasonal responses to the precipitation forcing (Section 4.2) and investigate whether the precipitation energy or flux is more significant for ozone loss (Section 5). In Section 5 we also test the ability of geomagnetic activity proxies to predict EMIC-EEP fluxes. Discussions and conclusions are presented in Section 6.

2 Instrumentation and models

The primary instrument used in this study is the Medium Energy Proton and Electron Detector (MEPED) suite of particle detectors carried by each satellite in the Polar-orbiting Operational Environmental Satellite (POES) constellation. Although the POES MEPED instruments are known to suffer from data quality issues, primarily detector cross-contamination (e.g., Yando et al., 2011), the POES constellation remains one of the best in-situ sources of medium-energy electron and proton precipitation data presently available.

The modern POES constellation consists of eight satellites (NOAA15–19 and METOP A–C) launched into low-Earth Sun-synchronous polar orbits between 1998–2018, the most recent of which, METOP-C, was launched in late 2018. Two of the POES satellites have since been decommissioned (NOAA-17 in 2013 and NOAA-16 in 2014). The MEPED instrument is comprised of eight particle detectors: four high-energy (> 16 MeV) omnidirectional proton detectors, two directional proton telescopes, and two directional electron telescopes. For this study, we only consider data from the directional detectors, i.e., the telescope pairs. For each of the MEPED directional detector pairs, one detector is aligned anti-parallel to the satellite's direction of motion, while the other points perpendicular to the first, radially outwards from the Earth – the 0° and 90° telescopes respectively. Depending on the location of a satellite in its orbit, each of these detectors will typically be dominated by trapped particles, bounce loss-cone (BLC) particles, drift loss-cone (DLC) particles, or some combination of the three (Rodger et al., 2010). For the L-shells considered in this study ($2 < L < 10$), the 0° telescopes will typically be measuring BLC/DLC particles, while the 90° telescopes will measure trapped fluxes.

Particle flux measured by the POES MEPED directional telescopes is accumulated over a 1 s period and binned by energy into three electron channels (E1–E3) in the nominal energy ranges > 30 keV, > 100 keV, and > 300 keV and proton fluxes in six energy bands from $30- > 6900$ keV (P1–P6). The MEPED instrument suffers significantly from cross-contamination (Yando et al., 2011), with the electron telescopes responding to proton flux and vice versa. In particular, the proton P6 channel responds strongly to relativistic (roughly > 800 keV) electrons. In the absence of high-energy protons, we are able to use the P6 proton channel as an ersatz electron detector; when using it in this way, it is sometimes referred to as the "E4" channel.

A detailed description of the POES satellite instruments can be found in Evans and Greer (2000).

2.1 Hendry et al. [2017] EMIC EEP database

In this study we investigate the impact that EMIC-driven EEP has on atmospheric chemistry using a database of 3777 EEP events extracted from the POES MEPED data by Hendry et al. (2016). This database was constructed using an algorithm derived by Carson et al. (2013) based on a previously identified EMIC precipitation signature (e.g., Miyoshi et al., 2008; Sandanger et al., 2009). This database has been shown by Hendry et al. (2016) to be strongly correlated with ground-based EMIC wave observations, confirming the link between these EEP events and EMIC wave activity. A follow-up study by Hendry et al. (2017) demonstrated that a significant proportion of these events showed significant EEP flux occurring at energies below 1 MeV. This was also confirmed by investigating RBSP observations at the time of these events, constraining the location, size, and energy range of EMIC-induced electron precipitation inferred from coincident precipitation data and relating them to the EMIC wave frequency, wave power, and ion band of the wave as measured in situ by the Van Allen Probes (Rodger et al., 2015).

Hendry et al. (2017) carried out an in-depth analysis of their precipitation trigger database, investigating the characteristics of the EMIC-driven EEP. Part of this analysis involved fitting a subset of the events in the database with an idealised flux energy distribution, which they called a "peaked" flux distribution:

$$j_{\text{peaked}}(E) = \left[e^{\alpha_1 - \beta_1 \ln E} + e^{-\alpha_2 + \beta_2 \ln E}\right]^{-1} \tag{1}$$

This distribution was derived from in-situ particle measurements from the Demeter satellite and theoretical analyses of EMIC-driven electron precipitation by Li et al. (2014). It is characterised by power-law growth and decay terms, controlled by the spectral indices $\beta_{1,2}$ and scaling factors $\alpha_{1,2}$. Combined, these produce a distribution peaked around a central energy E_p:

$$E_p = e^{(\alpha_1 + \ln \beta_1 + \alpha_2 - \ln \beta_2)/(\beta_1 + \beta_2)} \tag{2}$$

We note that an oversight in the analysis by Hendry et al. (2017) meant that some events were erroneously excluded from the fitting process due to an incorrectly implemented filter; we have corrected this analysis to include these events, giving 649 events analysed in total (in comparison to the 610 events reported in Hendry et al. (2017)). The inclusion of these extra events has not changed the results of Hendry et al. (2017) significantly.

2.1.1 Peak energy and total flux

The effect that electron precipitation has on atmospheric chemistry is strongly regulated by the energy of the precipitating electrons, as well as the flux magnitude. Electrons with higher energies are able to penetrate deeper into the atmosphere, driving the ionisation of atmospheric neutrals at lower altitudes than electrons with lower energies (Turunen et al., 2009). Clearly the number of precipitating electrons is also important, with a larger electron flux causing higher ionisation rates. For the fitted database events from Hendry et al. (2017), these two quantities are approximately characterised by the peak energy E_p, defined in Equation 2 above, and the total electron flux J, defined as:

$$J = \int_0^\infty j_{\text{peaked}}(E)\mathrm{d}E \tag{3}$$

$$\approx \sum_{E=0\ keV}^{E_{\max}} j_{\text{peaked}}(E)\Delta E \tag{4}$$

where we have approximated the infinite sum in Equation 3 as a finite sum over discrete energies from 0–10 MeV at 1 keV spacing.

Figure 1(a) shows the distribution of E_p for the 649 fitted electron precipitation events, binned according to a logarithmic scale in keV. We can see the same dual-population

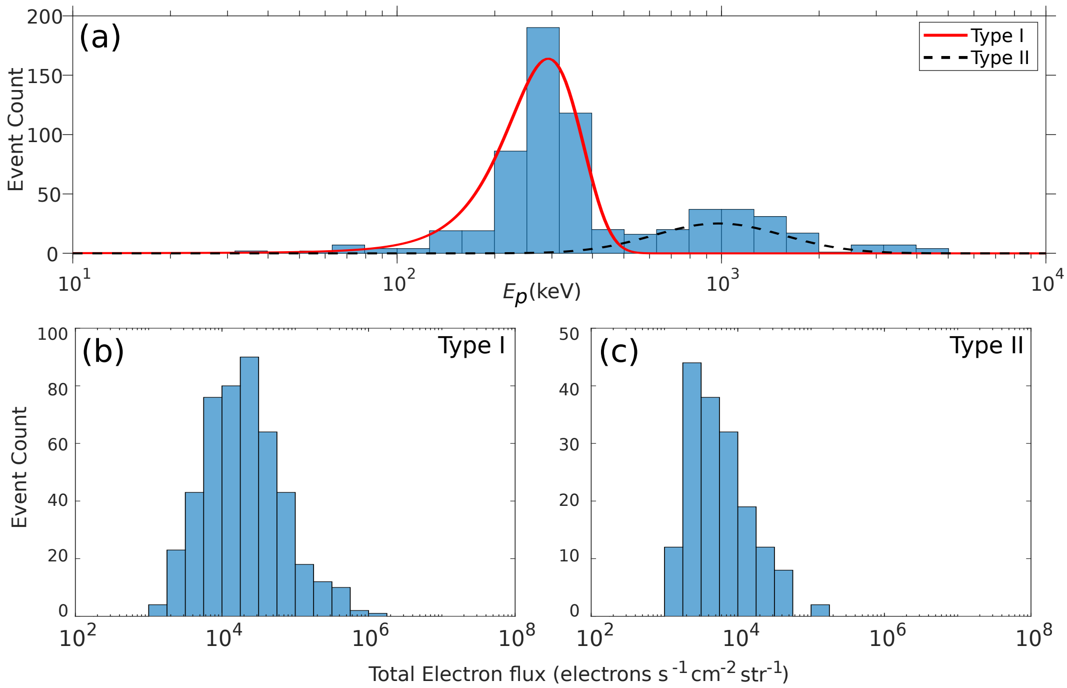

Figure 1. (a) Histogram of E_p values for the fitted database events, with the Type I distribution overlaid in red and the Type II distribution overlaid in dashed black. (b) and (c) Histogram of J values for the Type I and Type II events respectively.

as was seen in Figure 2 of Hendry et al. (2017). The dominant population, which we will call *Type I* events, has E_p values which occur between 100–600 keV and comprises around 71% of the fitted events; this group is roughly normally distributed (red line; median 292 keV). A smaller secondary population, which we will call *Type II* events, has E_p values in the 0.6–2 MeV range and makes up around 23% of the fitted events; this group is roughly log-normally distributed (black dashed line; median 1346 keV). Very few events ($< 3\%$) have $E_p > 2$ MeV. In J, the events as a whole are fairly evenly distributed between around $10^3 - 10^6$ electrons cm^{-2} sr^{-1} s^{-1}, with an average of around 1.24×10^4 electrons cm^{-2} sr^{-1} s^{-1}. Figures 1(b) and (c) show the distributions of J split between the Type I and Type II events respectively.

It is evident that Type II events on average have much lower J (median $10^{3.7}$ vs. $10^{4.3}$ electrons cm^{-2} sr^{-1} s^{-1}). This is due to the much smaller trapped flux populations at these energies, limiting the amount of flux that can possibly be lost. In contrast, the Type I events can access the much more populous $<$ 1 MeV trapped fluxes, allowing a much greater possible J.

We note that in Figure 1(c), there is a sharp drop off in event occurrence at J values around 10^3 electrons $\mathrm{cm}^{-2}\ \mathrm{sr}^{-1}\ \mathrm{s}^{-1}$, compared to the roughly normally distributed Type I events. This drop off is not natural, but is instead an artefact of the filtering of events with very small fluxes due to POES limitations (as described by Hendry et al. (2017)). If we assume that the "true" J distribution for Type II events has a similar shape to the Type I events, we might assume that the true Type II J distribution for an unfiltered database would extend down to $\sim 10^2$ electrons $\mathrm{cm}^{-2}\ \mathrm{sr}^{-1}\ \mathrm{s}^{-1}$.

It is worth reiterating the point raised by Hendry et al. (2017), that these fits are not necessarily unique. Due to the relatively small number of data points from POES, there may be multiple spectra that are able to reproduce the POES measured fluxes. In particular, the β_2 parameter, which controls the decay rate of the peaked spectrum at relativistic energies, is relatively poorly constrained at higher energies due to the lack of measurements from POES at these energies. This is unlikely to affect either E_p, which is tightly constrained by the relative flux of each electron channel, or J, due to the fact that the ultra-relativistic fluxes contribute only a small fraction of the total precipitated flux. However, it may impact our ability to look at energy-dependent effects; we will discuss this further in the next section.

In the current study, we will consider a small number of representative precipitation spectra from the Hendry et al. (2017) database of fitted events and investigate the potential impact of the observed precipitation on radiation belt trapped fluxes and the Earth's atmospheric chemistry.

3 Impact on the Radiation Belts

One of the most of important questions that arose from the Hendry et al. (2017) study was why this sub-MeV precipitation had not been reported in satellite data before, despite many years of study. One possible answer to this is that previous studies had been considering the data in the wrong order – starting with EMIC waves and then searching for EEP, as opposed to starting with EEP and looking for associated waves. Indeed, Qin et al. (2018) found that, when starting with EMIC waves and looking for EEP, only $\sim 25\%$ of events were positively associated with EEP, a rate just 10% higher than random coincidence. In comparison, Hendry et al. (2016) started with a specific type of EEP signature and found correlation with ground-based EMIC up to 90% of the time.

Another possible reason for the lack of sub-MeV EEP reports in the literature may lie with how these past studies were carried out. Electron precipitation is relatively difficult to study in-situ – at the magnetic equator, the bounce loss-cone (BLC) is very narrow, making it very difficult for equatorial satellites such as RBSP to resolve. Polar-orbiting satellites, such as POES and DEMETER, are better able to resolve pitch angles closer to the BLC – their orbits allow them to sample radiation belt fluxes much further down the field line, where the BLC is relatively large. The trade-off, however, is that the nature of these orbits mean that in any given orbit the satellites spend very limited time at the L-shells associated with EMIC-driven EEP. Experimental studies typically suggest EMIC L-shell extents of 0.1–1 ΔL (e.g., Mann et al., 2014; Hendry et al., 2020). For polar-orbiting satellites, this typically corresponds to a potential observation period of 10-20 s at best for any given event – depending on the temporal resolution of the instrument, this may correspond to only 2-3 data-points per event.

To get around the limitation of equatorial satellites for studying EEP, some studies have looked instead at the trapped flux populations, with the intent of detecting EMIC-driven changes in these fluxes, as opposed to the EEP itself. A seminal and oft-quoted example is the study by Usanova et al. (2014), who investigated the impact of EMIC-driven scattering on POES and RBSP-detected trapped fluxes. Usanova et al. reported that EMIC waves could cause the scattering of ultra-relativistic (> 2 MeV) electrons, but did not cause appreciable changes to < 1 MeV electron populations. This appears at first glance to be in direct conflict to the results of Hendry et al. (2017), who almost exclusively found events with EMIC-driven electron precipitation occurring at energies < 1 MeV. However, as we will show below, these two results are not necessarily contradictory.

3.1 Impact of EMIC-driven EEP on trapped flux populations

From the results of Hendry et al. (2017), we have a set of EMIC-driven EEP events from which we have derived peaked flux distributions (Eq. 1). These precipitating flux distributions paint a picture in which the vast majority of events drive significant electron population at relatively low energies (< 1 MeV). The question, then, is why do we typically see very little evidence of such low-energy precipitation through their impact on the trapped flux data? To answer this, we consider a simple test: given an idealised trapped flux distribution and given the precipitation spectra from Hendry et al. (2017), what changes in the trapped might we expect to see when we subtract this precipitation from the trapped fluxes?

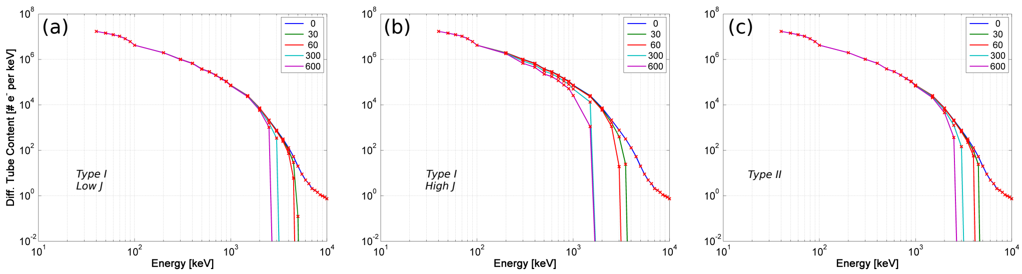

Figure 2. Evolution in time of the model flux distribution after EMIC-driven EEP for three different event categories: (a) Type I, low J; (b) Type I, high J; (c) Type II. The blue line indicates the baseline flux distribution (no precipitation), with the rest of the lines indicating progressively longer periods of EEP. The time periods are shown by differing colors at times givens in the legend.

Although we could in theory generate a “true” flux distribution by using data from the Van Allen probes, Arase, or similar satellites, for this thought-experiment we only need an idealised flux distribution. To obtain such a distribution, we use the AE9 radiation belt model (Johnston et al., 2017) to generate a sample realistic trapped electron flux distribution with energies from 40 keV to 10 MeV and pitch-angles from 0–90°. We integrate over the entire pitch-angle space to give us the total electron content in a flux-tube with 1 cm^2 area at 100 km for $L = 4.7$. From this generated trapped electron population, we can simply subtract the EMIC-driven energy-dependent EEP to estimate the impact on the trapped fluxes. By integrating Eq. (1) with respect to time, we can model the impact of this precipitation over an arbitrary length of time. We note that Eq. (1) is time-invariant — a more realistic approach would be to introduce some time-dependence to better model the decaying trapped flux. For this thought-experiment, however, a constant loss-rate is sufficient to determine the relative impact of the precipitation at different energies; a very similar approach was undertaken to investigate the long term impact of electron microburst precipitation on trapped electron fluxes by Douma et al. (2019).

Figure 2 represents the results of such an experiment, using flux distributions from three of the Hendry et al. (2017) events: two Type I events (a and b), and one Type II (c). These events, each with different α and β parameters, were chosen such that (a) has low flux ($J \sim 10^{3.8}$, $E_p = 248$ keV), (b) has high flux ($J \sim 10^{4.1}$, $E_p = 224$ keV), and (c) has average (for Type II) flux ($J \sim 10^{3.6}$, $E_p = 1012$ keV); in each case J has units of electrons $\mathrm{cm}^{-2}\ \mathrm{sr}^{-1}\ \mathrm{s}^{-1}$. These events correspond to events defined in the next section, with (a), (b), and (c) corresponding to events #1, #5, and #8 in Table 1 respectively. On each plot we show the unaffected trapped distribution (blue line) as well as the effects of the EEP after 30 s, 1 min, 5 min, and 10 min. The expected interaction time between electrons and EMIC waves is not exactly clear, as it depends not only on the energy of the electrons in question, but also strongly on the longitudinal extent of the EMIC wave region, which is in general fairly difficult to determine, and has to date largely only been examined on a case-by-case basis (e.g., Hendry et al., 2020).

The results shown in Figure 2 are rather striking. For all of the events shown, at ultra-relativistic energies we see almost complete depletion of the flux-tube. Although the scattered fluxes at these energies are relatively tiny compared to the lower energy scattered fluxes (at least 3-4 orders-of-magnitude lower), they constitute a large percentage of the total trapped flux at these energies, indicating that very strong scattering is occurring. Comparatively, at lower energies (i.e., < 1 MeV), we typically see almost no evidence of scattering at all, suggesting very inefficient scattering, with depletion rates of only 2% at 200 keV and $\sim 10\%$ at 300-400 keV. It is simply due to the several order-of-magnitude difference in the fluxes between the sub-relativistic and ultra-relativistic fluxes that the the precipitating fluxes peak at sub-relativistic energies, despite the primary electron dropouts occuring at relativistic energies.

As we mentioned in Section 2.1.1, the expected ultra-relativistic precipitating flux is strongly dependent on the spectral decay parameter β_2. The power-law nature of the peaked fit we have used means that relatively small changes in β_2 can result is significant changes in the loss-rate at ultra-relativistic energies. Thus, when interpretting these results one must keep in mind the possibility that the observed ultra-relativistic loss-rate could be faster or slower than reality, depending on whether we have under- or over-estimated the decay parameter β_2 in our fitting. With that said, the ability for EMIC-waves to rapidly scatter the ultra-relativistic portion of the radiation belts is well-established in the literature, both theoretically (e.g. Kubota & Omura, 2017; Hendry et al., 2019) and experimentally (e.g. Usanova et al., 2014; Shprits et al., 2016). As a result, our conclusion — that ultra-relativistic fluxes are depleted at a much more rapid rate than sub-MeV fluxes — is likely not significantly affected by this uncertainty.

This result largely explains the apparent contradiction between EMIC studies looking at trapped and precipitating electrons. In studies such as Usanova et al. (2014), it is likely that the sub-relativistic electron precipitation seen by Hendry et al. (2017) is in fact present, however the relatively small decrease in total flux due at these energies combined with the relatively long time-scales investigated (i.e., weeks) means that there simply isn't the resolution required to observe these changes. We suggest that the conclusion to be drawn from this will depend on ones primary focus; if the goal is to understand the scattering process or precipitation levels into the atmosphere, the sub-relativistic precipitating fluxes are important. However, if the goal is to predict the variation of trapped fluxes, those sub-relativistic energies are considerably less significant, while the ultra-relativistic changes are dramatic.

4 Atmospheric Impact

We now turn our attention to the Earth's atmosphere; given that the events studied by Hendry et al. (2016) and Hendry et al. (2017) events are occurring, and that these events include precipitation spanning a very wide range of energies, how important are they to the Earth's atmospheric chemistry? To examine this, we consider the atmospheric ionisation rates expected from these events and the resulting changes to neutral atmospheric chemistry driven by this ionisation.

An analysis of all 649 fitted events from the Hendry et al. (2017) database is outside the scope of this study — instead, we consider 9 representative events from the database such that the range of parameters observed across the database are included. We use the same categorisation as earlier, i.e., Type I or Type II events. We roughly divide the Type I these events into two groups based on their total flux J: small events ($J \sim 10^{3.5} - 10^{4.5}$) and large events $J \sim 10^{4.5} - 10^{5.5}$, both in electrons $\mathrm{cm}^{-2}\ \mathrm{sr}^{-1}\ \mathrm{s}^{-1}$. For Type II events there is not as much spread in J, so we do not subdivide these further. For each

Table 1. Spectral parameters of Equation 1, E_p (keV) and J (electrons cm^{-2} sr^{-1} s^{-1}), for the representative event spectra.

	#	α_1	β_1	α_2	β_2	E_p	J
Type I	1	34	6.9	10.8	1.5	248	5.9×10^3
	2	31	6.4	17.5	2.4	276	1.3×10^4
	3	35	7.1	13.8	1.8	281	1.5×10^4
	4	31	6.4	9.9	1.2	271	1.8×10^4
	5	32.9	7.2	14.4	1.8	224	3.3×10^4
	6	23.8	5.1	24.4	3.3	327	3.6×10^4
Type II	7	43.5	6.7	9.7	1.3	949	4.0×10^3
	8	46.9	7.1	14.8	2.0	1012	4.0×10^3
	9	50.3	7.2	25.8	3.4	1408	2.4×10^3

of these three subsets, we selected events that represented the spread of spectral parameters (i.e., $\alpha_1, \beta_1, \alpha_2, \beta_2$) seen in the group, giving us a total of nine events to consider. These events are summarised in Table 1 – for ease of reference, we assign each event a numerical index.

4.1 Ionisation rate calculations

We calculate the ionisation rates for each of our spectra using the method described in Section 2.4 of Rodger et al. (2012), using Halley, Antarctica (75° S, 26° W, $L \approx 4.5$) as our modelling point. We investigate both the summer and winter atmospheres, modeled on 22 December 2004 and 22 June 2004 respectively. Each energy spectra is modeled as a discretised collection of mono-energetic electron beams; for each of these beams, an altitude specific energy deposition is found. The total energy deposition for the event is found by integrating across the entire energy range of the spectrum (10–10000 keV). The resulting altitude specific energy deposition for the entire spectrum is then divided by the ionisation energy of a single molecule, which is taken to be ∼35 eV (Rees & Rees, 1989), to give an altitude-dependent ionisation rate.

For each of the ionisation rate profiles calculated using the above technique, both day-time (18:00 UT, 12:00 LT) and night-time (06:00 UT, 00:00 LT) atmospheres were considered. In all cases, the day and night ionisation rates were indistinguishable by eye, and so we have taken them to be essentially identical. For all of the following considerations, we will be using the night-time ionisation rates.

4.2 Modeling the atmospheric impact

To simulate the EMIC precipitation impact on the atmosphere we use the 1-D Sodanlylä Ion and neutral Chemistry model (SIC). This model has been described in detail by Verronen et al. (2005, 2016); Turunen et al. (2009) and was recently used by Seppälä et al. (2018) to carry out an analogous study of the atmospheric impact of relativistic electron microbursts. Here we will summarize some of the main features of the model. The model solves the impact of EEP ionisation on 34 atmospheric neutrals, including HO_x, NO_x, and ozone, and several ionized species in the altitude range from 20 km to 150 km by solving several hundred ion-chemistry reactions. The model accounts for external forcing due to solar UV and soft X-ray radiation, as well as ionisation from electron and proton precipitation, and galactic cosmic rays. The model simulations for this study were run with 5 min time step for the same location as the ionisation calculations described above, for both a summer and winter atmosphere. We first perform simulations without any EMIC precipitation, which provide a "background" level for us to contrast our EMIC simulations against. Times from the model outputs corresponds to UT, with the EMIC precipitation starting at UT midnight.

Statistical information on the duration of EMIC-related EEP events is fairly sparse in the literature; the events as observed in POES last only seconds, but these represent just brief snapshots of the events as the satellites fly through the precipitation region. Ground-based case-study observations of EMIC-driven EEP show durations ranging from tens of minutes (e.g., Hendry et al., 2016) to several hours (e.g., Clilverd et al., 2015), typically with a fairly smooth ramp up and down in intensity as the precipitation footprint passes over the region of interest. We allow the EEP to drive our model for an hour, applying a Gaussian window to the ionisation to simulate the smooth variation seen in observational studies. In other words, the precipitation increases from zero at 00:00 UT to a peak at 00:30 UT, returning to zero again at 01:00 UT.

Although the ionisation of the atmosphere sets off a raft of chemical changes, the most important changes for our purposes are the relative increases in HO_x and NO_x, both of which can lead to the catalytic destruction of ozone (M. Andersson et al., 2014). HO_x has a very short chemical lifetime under all conditions, due to rapid self-annihilation, however NO_x is mainly lost from the atmosphere by photolysis in the presence of sunlight. Thus, during the polar winter EEP can result in accumulation of NO_x, which can subsequently be transported to lower altitudes where it can have a delayed effect on stratospheric ozone balance (the so called EPP-indirect effect). The importance of sunlight in regulating the atmospheric chemical balance via photolysis means that we expect significant differences in the chemical response of the atmosphere in summer and winter; we will thus consider these periods separately.

4.2.1 Summer response

Figure 3 shows three of the Summer modeling runs, representing small, medium, and strong atmospheric responses (events #9, #2, and #5 from Table 1 respectively; similar plots for the rest of the runs can be found in the Supplementary Material). As can be seen in this figure, EMIC-driven EEP into the summer polar atmosphere can, for the largest events, drive significant increases in relative HO_x and NO_x concentrations. Due to rapid dissociation, however, these increases are short-lived. In the case of NO_x, the changes lasted little more than a day, while for HO_x levels returned to baseline within ~ 30 min. Nonetheless, we see significant decreases in relative ozone concentrations, with $\sim 10\%$ decreases seen for the larger events. As with the catalysts, however, these losses are short-lived, returning to baseline within roughly 2 hours.

4.2.2 Winter response

Figure 4 shows the impact of the same events in Figure 3 on a Winter atmosphere (see the Supplementary Material for the full results). The changes to HO_x are the most dramatic, with relative increases of several thousand percent over the reference atmosphere (this is expected as during winter the background levels of HO_x are generally lower than during summer). Even in the absence of sunlight these increases are short-lived, however, due to rapid self-annihilation – typically, these HO_x increases return to baseline by the end of the simulation period. The relative increases in NO_x are smaller, peaking at only 100-200% increases over baseline, but are much more resilient. As NO_x is primarily destroyed by photo-dissociation, the lack of significant levels of sunlight in the

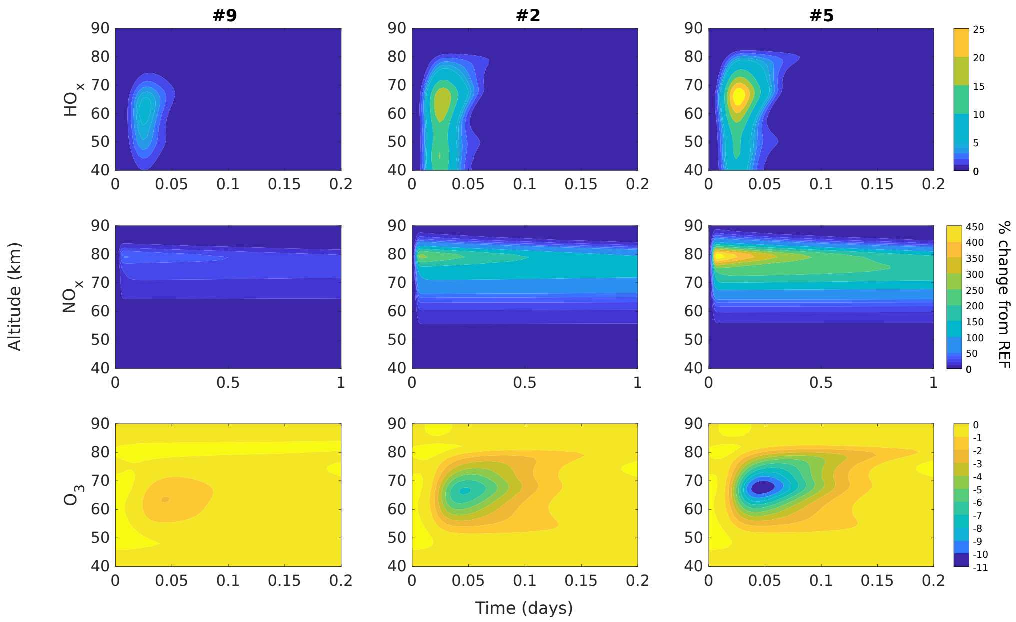

Figure 3. Relative change in HO_x (top), NO_x (middle), and O_3 (bottom) relative to the reference run in response to EMIC-driven EEP during the Summer months for events #9, #2, and #5 from Table 1. Note that the NO_x plots are plotted on a longer time scale to show the slower dissociation compared to HO_x.

polar winter means that for most of the events modelled, there remains significantly increased levels of NO_x even five days after the event.

As is to be expected, these significant increase in HO_x and NO_x result in destruction of mesospheric ozone, with relative decreases of $\sim 10\%$ seen in the larger events. Although these generally appear to be smaller than the decreases during summer, during winter the ozone loss persists for much longer, with significant decreases present even several days after the event. With repeated EMIC-driven EEP events, this could lead to significant impact on ozone balance over the duration of an entire winter.

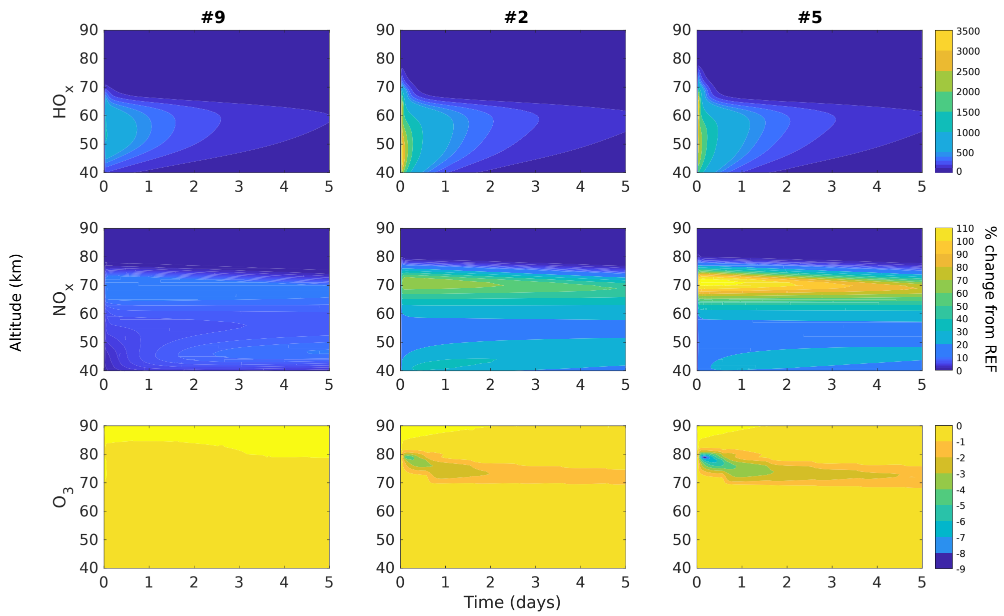

Figure 4. As with Figure 3, but for the Winter months and extended out to show the full 5-day simulation period.

5 Ozone loss: correlations with E_p and J

In this study, we have considered only a small sample of EMIC-driven EEP events. The question remains, then, as to how we extend these results to, for instance, the entirety of the Hendry et al. (2017) database of fit events, or indeed to EMIC-driven EEP events as a whole? To answer this, we look at how the response of the atmosphere varies with the key parameters of the Hendry et al. (2017) fit events, the peak energy E_p and the total flux J. Due to the relatively small response that we observed from the summer atmosphere, and due to the potential for winter accumulation of NO_x, we focus primarily on the response of the winter atmosphere.

From Figure 4, we can see that the majority of the ozone loss, at least initially, occurs at altitudes of around 80 km, later dropping down closer to 75 km. We know from analysis of electron penetration depth (see for instance Figure 3 of Turunen et al. (2009)) that ionisation at this altitude is driven primarily by electrons with energies > 100 keV. Given that all of our events have E_p well above this, it is thus unsurprising that, based on a simple linear regression calculation, there is no dependence of the maximum decrease in ozone on E_p ($p = 0.093, R^2 = 0.35$, where R is the Pearson correlation coefficient). The same also applies to the increases in NO_x ($p = 0.097, R^2 = 0.343$) and HO_x ($p = 0.332, R^2 = 0.134$).

As a result of this, we can assume that almost every precipitating electron in these EMIC events must pass through the altitude region where peak ozone loss occurs. It is perhaps unsurprising, then, that we find a very strong linear relationship between the calculated relative ozone loss and the total flux J ($p = 4.1 \times 10^{-7}, R^2 = 0.979$). We see a similarly strong relation between J and the relative increase in NO_x ($p = 1.6 \times 10^{-6}, R^2 = 0.969$); the relationship with HO_x is weaker ($p = 0.038, R^2 = 0.482$), but still statistically significant. This suggests that all of the variations in ozone and NO_x, and at least some of variations in HO_x, are driven by variations in J.

It is important to note that this result — a strong dependence on J — means that the analysis presented in this section is likely unaffected by the uncertainty in the ultra-relativistic loss-rate mentioned in Section 2.1.1. Any changes to the total flux J due to increases or decreases in the ultra-relativistic loss-rate will be largely negligible, due to the several orders-of-magnitude greater flux seen at the lower energies.

Given the clear dependence on J, it is instructive to consider whether this dependence is necessarily reflected by coarser measures of geomagnetic activity, for instance the geomagnetic index K_p. It has been previously established (Carson et al., 2013) that there is a strong, roughly linear relationship between K_p and the occurrence of precipitation events such as those in the Hendry et al. (2017) database, with a higher frequency of events occurring at higher K_p. However, we find no such dependence between the total flux J and K_p – comparing the calculated J for the entire Hendry et al. (2017) database with the instantaneous K_p shows that variation in K_p explains almost none of the variation in the total flux J ($p = 1.6 \times 10^{-6}, R^2 = 0.04$). We see a similar result for the derived index A_p ($p = 1.3 \times 10^{-13}, R^2 = 0.08$). This is of particular interest due to the A_p index's use as a proxy for EEP in climate modeling (e.g., Matthes et al., 2017). The fact that there is no clear relation between J and A_p suggests that EMIC-driven EEP is not being accounted for in these models.

6 Discussion and conclusions

By studying the impact of the Hendry et al. (2017) EEP spectra on simulated trapped flux distributions, we've shown that not only can these spectra cause significant depletion at ultra-relativistic energies, consistent with experimental and theoretical analyses, but also that these events do not cause significant radiation belt depletion at sub-MeV energies. This has interesting implications. Importantly, it explains the apparent contradiction between studies looking solely at the depletion of trapped electron fluxes and those looking at loss-cone fluxes directly – it is not that the sub-MeV precipitation is not occurring, but rather that the lost electrons represent only a tiny fraction of the total electron population at these energies. As a result, at the typical flux resolution of equatorial satellites and temporal resolution of trapped flux studies (e.g., Usanova et al., 2014), it is all but impossible to resolve the changes in sub-MeV flux caused by EMIC-driven scattering.

In addition to resolving this apparent contradiction, our results also provide an indication of the relative electron scattering efficiency by EMIC waves at ultra-relativistic and sub-MeV energies. Figure 2 shows the incredibly efficient removal of ultra-relativistic electrons, with significant depletion of the population after only ~ 1 min. In comparison, the 300-400 keV electron population is barely affected, even after 10 min of scattering. This may mean that whatever interaction process is driving the sub-MeV electron precipitation for these events is a remarkably inefficient, unable to effectively interact with the majority of the electron population at these energies. For instance, it may be that the sub-MeV electrons are below the resonance energy of a particular EMIC wave, but are able to be weakly scattered by off-resonant or non-resonant interactions with the wave. It would be instructive to compare the Hendry et al. (2017) EEP spectra with calculations of minimum resonant energies to determine if these sub-MeV spectra are indeed due to off- or non-resonant interactions. Such calculations have been calculated for individual case-studies; for instance, evidence of weak, off-resonant interactions were apparent in the case study of Hendry et al. (2019), but these were not investigated in detail. Unfortunately, the calculation of the minimum resonance energy for these events requires in-situ wave measurements, which are typically not available. This makes large-scale investigations in this manner all but impossible. Further investigation is still required to properly understand the complex interactions between EMIC waves and electrons at all energies.

It should be noted that there *are* examples in the literature of significant trapped electron depletions occurring at sub-MeV energies. For instance, the studies by Rodger et al. (2015) and Hendry et al. (2019) both observed significant electron depletion down to hundreds of keV in RBSP MagEIS data. In these instances this was due to plasma conditions driving the minimum resonance energy down to sub-MeV energies (500 keV in the case of Hendry et al. (2019)), allowing for efficient scattering at much lower energies than is typical for EMIC. It is unclear if depletions such as these would be visible in studies such as Usanova et al. (2014), due broad time range considered in these studies. If the radiation belts are rapidly refilled by sub-MeV electrons after their depletion by EMIC waves, then the dropouts would not be visible on longer time scales. Indeed, in their case study Hendry et al. (2019) observed at least a partial refilling of the radiation belts only 6 hrs after an EMIC-driven depletion. A possible explanation is related to the fact that EMIC waves often occur during periods of significant substorm activity (Remya et al., 2018). The resulting substorm particle injections from the magnetospheric tail region can then set off a chain-reaction of processes that lead to the rapid replenishment of the lost electron populations, refilling the radiation belts at sub-MeV energies.

We have shown that, based on the EMIC EEP spectra produced by Hendry et al. (2017), EMIC-driven electron precipitation can have a significant effect on the chemical balance of the Earth's atmosphere. The levels of ozone depletion that we see are not particularly large when compared to other similar EEP sources such as microbursts, which were shown through similar analysis to cause up to 20% ozone loss (Douma et al., 2017); however, EMIC waves are known to occur fairly regularly. Based on the database of precipitation triggers from Hendry et al. (2017), we expect to see an EMIC-driven EEP event on average every 10 hours, with events less frequent during solar minimum (e.g., most of 2009), and more frequent during solar maximum.

Although this is by no means a perfect measure of EMIC-driven EEP occurrence, even if an EEP-driving EMIC event only occurred on average every day, or even every second day, this constant ionisation of the atmosphere combined with the slow dissociation of NO_x during polar winter could lead to significant accumulation of this catalyst during the winter months. Thus, EMIC-driven EEP is potentially an important, but thus far unaccounted for, factor in polar atmospheric ozone balance.

Our results suggest that EMIC-driven EEP is significant enough that it should be considered as a source of EEP in atmospheric chemical models. However, it would appear that this precipitation is not being properly accounted for by existing EEP proxy methods. Further work is needed in this area to derive an appropriate proxy not only for EMIC-driven EEP occurrence, but also the intensity of these events.

Clearly there is much we still don't understand about EMIC waves, and in particular their interaction with radiation belt electrons. In this paper, however, we have answered one of the major contradictions that appeared in the literature regarding the influence that EMIC waves have on sub-MeV and ultra-relativistic electrons. We have also shown that, while an individual EMIC event does not have a large impact on the radiation, the cumulative effect is likely to cause significant, and potentially experimentally detectable, effects on the polar atmosphere.

Acknowledgments

The authors wish to thank the personnel who developed, maintain, and operate the NOAA/METOP/POES spacecraft. The POES data used in this paper are available at NOAA's National Geophysical Data Center (https://satdat.ngdc.noaa.gov/sem/poes/). ATH would like to acknowledge the support of the postdoctoral program of the Czech Academy of Sciences. MAC would like to acknowledge support for this work from the Natural Environment Research Council, NERC Highlight Topic Grant #NE/P01738X/1 (Rad-Sat).

References

Andersson, M., Verronen, P., Rodger, C., Clilverd, M., & Seppälä, A. (2014). Missing driver in the Sun–Earth connection from energetic electron precipitation impacts mesospheric ozone. *Nature communications*, *5*.

Andersson, M. E., Verronen, P. T., Rodger, C. J., Clilverd, M. A., & Wang, S. (2014). Longitudinal hotspots in the mesospheric OH variations due to energetic electron precipitation. *Atmospheric Chemistry and Physics*, *14*(2), 1095–1105.

Carson, B. R., Rodger, C. J., & Clilverd, M. A. (2013). POES satellite observations of EMIC-wave driven relativistic electron precipitation during 1998-2010. *Journal of Geophysical Research: Space Physics*, *118*(1), 232–243. Retrieved from http://dx.doi.org/10.1029/2012JA017998 doi: 10.1029/2012JA017998

Chen, L., Thorne, R. M., Bortnik, J., & Zhang, X.-J. (2016). Nonresonant interactions of electromagnetic ion cyclotron waves with relativistic electrons. *Journal of Geophysical Research: Space Physics*, *121*(10), 9913–9925. Retrieved from http://dx.doi.org/10.1002/2016JA022813 doi: 10.1002/2016JA022813

Clausen, L. B. N., Baker, J. B. H., Ruohoniemi, J. M., & Singer, H. J. (2011). EMIC waves observed at geosynchronous orbit during solar minimum: Statistics and excitation. *Journal of Geophysical Research: Space Physics*, *116*(A10). Retrieved from http://dx.doi.org/10.1029/2011JA016823 doi: 10.1029/2011JA016823

Clilverd, M. A., Duthie, R., Hardman, R., Hendry, A. T., Rodger, C. J., Raita, T., ... Milling, D. K. (2015). Electron precipitation from EMIC waves: A case study from 31 May 2013. *Journal of Geophysical Research: Space Physics*, *120*(5), 3618–3631. Retrieved from http://dx.doi.org/10.1002/2015JA021090 doi: 10.1002/2015JA021090

Denton, R., Ofman, L., Shprits, Y., Bortnik, J., Millan, R., Rodger, C., ... Komar, C. (2019). Pitch angle scattering of sub-MeV relativistic electrons by electromagnetic ion cyclotron waves. *Journal of Geophysical Research: Space Physics*, *0*(ja). Retrieved from https://agupubs.onlinelibrary.wiley.com/doi/abs/10.1029/2018JA026384 doi: 10.1029/2018JA026384

Douma, E., Rodger, C. J., Blum, L. W., & Clilverd, M. A. (2017). Occurrence characteristics of relativistic electron microbursts from SAMPEX observations. *Journal of Geophysical Research: Space Physics*. Retrieved from http://dx.doi.org/10.1002/2017JA024067 doi: 10.1002/2017JA024067

Douma, E., Rodger, C. J., Blum, L. W., O'Brien, T. P., Clilverd, M. A., & Blake, J. B. (2019). Characteristics of Relativistic Microburst Intensity From SAM-

PEX Observations. *Journal of Geophysical Research: Space Physics*, *124*(7), 5627-5640. Retrieved from https://agupubs.onlinelibrary.wiley.com/doi/abs/10.1029/2019JA026757 doi: 10.1029/2019JA026757

Evans, D. S., & Greer, M. S. (2000). *Polar Orbiting Environmental Satellite Space Environment Monitor-2: Instrument Description and Archive Data Documentation.* US Department of Commerce, National Oceanic and Atmospheric Administration, Oceanic and Atmospheric Research Laboratories, Space Environment Center.

Friedel, R. H. W., Reeves, G. D., & Obara, T. (2002). Relativistic electron dynamics in the inner magnetosphere—A review. *Journal of Atmospheric and Solar-Terrestrial Physics*, *64*(2), 265–282.

Gendrin, R., Lacourly, S., Troitskaya, V., Gokhberg, M., & Shepetnov, R. (1967). Caracteristiques des pulsations irregulieres de periode decroissante (ipdp) et leurs relations avec les variations du flux des particules piegees dans la magnetosphere. *Planetary and Space Science*, *15*(8), 1239–1240.

Gordon, E. M., Seppälä, A., Funke, B., Tamminen, J., & Walker, K. A. (2020). Observational evidence of EPP-NO_x interaction with chlorine curbing Antarctic ozone loss. *Atmos. Chem. Phys. Discuss.*. (in review) doi: 10.5194/acp-2020-847

Gordon, E. M., Seppälä, A., & Tamminen, J. (2020). Evidence for energetic particle precipitation and quasi-biennial oscillation modulations of the Antarctic NO_2 springtime stratospheric column from OMI observations. *Atmos. Chem. Phys.*, *20*(11), 6259–6271. doi: 10.5194/acp-20-6259-2020

Hendry, A. T., Rodger, C. J., & Clilverd, M. A. (2017). Evidence of sub-MeV EMIC-driven electron precipitation. *Geophysical Research Letters*, *44*(3), 1210–1218. Retrieved from http://dx.doi.org/10.1002/2016GL071807 doi: 10.1002/2016GL071807

Hendry, A. T., Rodger, C. J., Clilverd, M. A., Engebretson, M. J., Mann, I. R., Lessard, M. R., ... Milling, D. K. (2016). Confirmation of EMIC wave driven relativistic electron precipitation. *Journal of Geophysical Research: Space Physics*. Retrieved from http://dx.doi.org/10.1002/2015JA022224 doi: 10.1002/2015JA022224

Hendry, A. T., Santolik, O., Kletzing, C. A., Rodger, C. J., Shiokawa, K., & Baishev, D. (2019). Multi-instrument Observation of Nonlinear EMIC-Driven Electron Precipitation at sub–MeV Energies. *Geophysical Research Letters*, *46*(13), 7248-7257. Retrieved from `https://agupubs.onlinelibrary.wiley.com/doi/abs/10.1029/2019GL082401` doi: 10.1029/2019GL082401

Hendry, A. T., Santolik, O., Miyoshi, Y., Matsuoka, A., Rodger, C. J., Clilverd, M. A., . . . Shinohara, I. (2020). A Multi-Instrument Approach to Determining the Source-Region Extent of EEP-Driving EMIC Waves. *Geophysical Research Letters*, *47*(7), e2019GL086599. Retrieved from `https://agupubs.onlinelibrary.wiley.com/doi/abs/10.1029/2019GL086599` doi: 10.1029/2019GL086599

Jacobs, J. A. (1970). *Geomagnetic micropulsations* (Vol. 1). Springer-Verlag Berlin Heidelberg. doi: 10.1007/978-3-642-86828-3

Johnston, W. R., O'Brien, T. P., Ginet, G., Huston, S., Guild, T., Roth, C., . . . et al. (2017). Irene: AE9/AP9/SPM radiation environment model. *Users Guide, version 1.20.001*.

Kubota, Y., & Omura, Y. (2017). Rapid precipitation of radiation belt electrons induced by EMIC rising tone emissions localized in longitude inside and outside the plasmapause. *Journal of Geophysical Research: Space Physics*, *122*(1), 293-309. Retrieved from `https://agupubs.onlinelibrary.wiley.com/doi/abs/10.1002/2016JA023267` doi: 10.1002/2016JA023267

Li, Z., Millan, R. M., Hudson, M. K., Woodger, L. A., Smith, D. M., Chen, Y., . . . Spence, H. E. (2014). Investigation of EMIC wave scattering as the cause for the BARREL 17 January 2013 relativistic electron precipitation event: A quantitative comparison of simulation with observations. *Geophysical Research Letters*, *41*(24), 8722–8729. Retrieved from `http://dx.doi.org/10.1002/2014GL062273` doi: 10.1002/2014GL062273

Mann, I. R., Usanova, M. E., Murphy, K., Robertson, M. T., Milling, D. K., Kale, A., . . . Raita, T. (2014). Spatial localization and ducting of EMIC waves: Van Allen Probes and ground-based observations. *Geophysical Research Letters*, *41*(3), 785–792. Retrieved from `http://dx.doi.org/10.1002/2013GL058581` doi: 10.1002/2013GL058581

Matthes, K., Funke, B., Andersson, M. E., Barnard, L., Beer, J., Charbonneau, P., . . . others (2017). Solar forcing for CMIP6 (v3. 2). *Geoscientific Model*

Development, *10*(6), 2247.

Meredith, N. P., Thorne, R. M., Horne, R. B., Summers, D., Fraser, B. J., & Anderson, R. R. (2003). Statistical analysis of relativistic electron energies for cyclotron resonance with EMIC waves observed on CRRES. *Journal of Geophysical Research: Space Physics*, *108*(A6). Retrieved from `http://dx.doi.org/10.1029/2002JA009700` doi: 10.1029/2002JA009700

Millan, R., & Thorne, R. (2007). Review of radiation belt relativistic electron losses . *Journal of Atmospheric and Solar-Terrestrial Physics*, *69*(3), 362 - 377. Retrieved from `http://www.sciencedirect.com/science/article/pii/S1364682606002768` doi: http://dx.doi.org/10.1016/j.jastp.2006.06.019

Millan, R. M., Lin, R. P., Smith, D. M., & McCarthy, M. P. (2007). Observation of relativistic electron precipitation during a rapid decrease of trapped relativistic electron flux. *Geophysical research letters*, *34*(10).

Miyoshi, Y., Sakaguchi, K., Shiokawa, K., Evans, D., Albert, J., Connors, M., & Jordanova, V. (2008). Precipitation of radiation belt electrons by EMIC waves, observed from ground and space. *Geophysical Research Letters*, *35*(23). Retrieved from `http://dx.doi.org/10.1029/2008GL035727` doi: 10.1029/2008GL035727

Newnham, D. A., Clilverd, M. A., Rodger, C., Hendrickx, K., Megner, L., Kavanagh, A. J., ... others (2018). Observations and modeling of increased nitric oxide in the antarctic polar middle atmosphere associated with geomagnetic storm-driven energetic electron precipitation. *Journal of Geophysical Research: Space Physics*, *123*(7), 6009–6025.

Omura, Y., & Zhao, Q. (2013). Relativistic electron microbursts due to nonlinear pitch angle scattering by EMIC triggered emissions. *Journal of Geophysical Research: Space Physics*, *118*(8), 5008–5020.

Qin, M., Hudson, M., Millan, R., Woodger, L., & Shekhar, S. (2018). Statistical Investigation of the Efficiency of EMIC Waves in Precipitating Relativistic Electrons. *Journal of Geophysical Research: Space Physics*, *123*(8), 6223-6230. Retrieved from `https://agupubs.onlinelibrary.wiley.com/doi/abs/10.1029/2018JA025419` doi: 10.1029/2018JA025419

Randall, C. E., Harvey, V. L., Singleton, C. S., Bernath, P. F., Boone, C. D., & Kozyra, J. U. (2006). Enhanced NO_x in 2006 linked to strong upper stratospheric Arctic vortex. *Geophys. Res. Lett.*, *33*, L18811. doi: 10.1029/2006GL027160

Rees, M. H., & Rees, N. (1989). *Physics and chemistry of the upper atmosphere* (Vol. 1). Cambridge University Press.

Remya, B., Sibeck, D. G., Halford, A. J., Murphy, K. R., Reeves, G. D., Singer, H. J., … Thaller, S. A. (2018). Ion injection triggered EMIC waves in the earth's magnetosphere. *Journal of Geophysical Research: Space Physics*, *123*(6), 4921-4938. Retrieved from `https://agupubs.onlinelibrary.wiley.com/doi/abs/10.1029/2018JA025354` doi: 10.1029/2018JA025354

Rodger, C. J., Carson, B. R., Cummer, S. A., Gamble, R. J., Clilverd, M. A., Green, J. C., … Berthelier, J.-J. (2010). Contrasting the efficiency of radiation belt losses caused by ducted and nonducted whistler-mode waves from ground-based transmitters. *Journal of Geophysical Research: Space Physics (1978–2012)*, *115*(A12).

Rodger, C. J., Clilverd, M. A., Kavanagh, A. J., Watt, C. E. J., Verronen, P. T., & Raita, T. (2012). Contrasting the responses of three different ground-based instruments to energetic electron precipitation. *Radio Science*, *47*(2). Retrieved from `http://dx.doi.org/10.1029/2011RS004971` doi: 10.1029/2011RS004971

Rodger, C. J., Clilverd, M. A., Thomson, N. R., Gamble, R. J., Seppälä, A., Turunen, E., … Berthelier, J.-J. (2007). Radiation belt electron precipitation into the atmosphere: Recovery from a geomagnetic storm. *Journal of Geophysical Research: Space Physics*, *112*(A11).

Rodger, C. J., Hendry, A. T., Clilverd, M. A., Kletzing, C. A., Brundell, J. B., & Reeves, G. D. (2015). High-resolution In-situ Observations of Electron Precipitation-Causing EMIC Waves. *Geophysical Research Letters*. Retrieved from `http://dx.doi.org/10.1002/2015GL066581` doi: 10.1002/2015GL066581

Sandanger, M., Søraas, F., Sørbø, M., Aarsnes, K., Oksavik, K., & Evans, D. (2009). Relativistic electron losses related to EMIC waves during CIR and CME storms . *Journal of Atmospheric and Solar-Terrestrial Physics*, *71*(10-11), 1126 - 1144. Retrieved from `http://www.sciencedirect.com/science/article/pii/S1364682608001946` doi: 10.1016/j.jastp.2008.07.006

Seppälä, A., Douma, E., Rodger, C., Verronen, P., Clilverd, M. A., & Bortnik, J. (2018). Relativistic electron microburst events: Modeling the atmospheric impact. *Geophysical Research Letters*, *45*(2), 1141–1147.

Seppälä, A., Matthes, K., Randall, C. E., & Mironova, I. A. (2014). What is the solar influence on climate? Overview of activities during CAWSES-II. *Prog. Earth Planet. Sci.*, *1*(1), 24. doi: 10.1186/s40645-014-0024-3

Seppälä, A., Randall, C. E., Clilverd, M. A., Rozanov, E., & Rodger, C. J. (2009). Geomagnetic activity and polar surface air temperature variability. *Journal of Geophysical Research: Space Physics (1978–2012)*, *114*(A10).

Shprits, Y. Y., Drozdov, A. Y., Spasojevic, M., Kellerman, A. C., Usanova, M. E., Engebretson, M. J., … others (2016). Wave-induced loss of ultra-relativistic electrons in the van allen radiation belts. *Nature communications*, *7*(1), 1–7.

Thorne, R. M. (2010). Radiation belt dynamics: The importance of wave-particle interactions. *Geophysical Research Letters*, *37*(22). Retrieved from `http://dx.doi.org/10.1029/2010GL044990` doi: 10.1029/2010GL044990

Turunen, E., Verronen, P. T., Seppälä, A., Rodger, C. J., Clilverd, M. A., Tamminen, J., … Ulich, T. (2009). Impact of different energies of precipitating particles on NOx generation in the middle and upper atmosphere during geomagnetic storms. *Journal of Atmospheric and Solar-Terrestrial Physics*, *71*(10), 1176 - 1189. Retrieved from `http://www.sciencedirect.com/science/article/pii/S1364682608001958` doi: https://doi.org/10.1016/j.jastp.2008.07.005

Usanova, M. E., Drozdov, A., Orlova, K., Mann, I. R., Shprits, Y., Robertson, M. T., … Wygant, J. (2014). Effect of EMIC waves on relativistic and ultrarelativistic electron populations: Ground-based and Van Allen Probes observations. *Geophysical Research Letters*, *41*(5), 1375–1381. Retrieved from `http://dx.doi.org/10.1002/2013GL059024` doi: 10.1002/2013GL059024

van de Kamp, M., Rodger, C., Seppälä, A., Clilverd, M. A., & Verronen, P. (2018). An updated model providing long-term data sets of energetic electron precipitation, including zonal dependence. *Journal of Geophysical Research: Atmospheres*, *123*(17), 9891–9915.

Verronen, P. T., Andersson, M. E., Marsh, D. R., Kovacs, T., & Plane, J. M. C. (2016). WACCM-D Whole Atmosphere Community Climate Model with

D-region ion chemistry. *J. Adv. Mod. Earth Sys.*, *8*(2), 954–975. doi: 10.1002/2015MS000592

Verronen, P. T., Seppälä, A., Clilverd, M. A., Rodger, C. J., Kyrölä, E., Enell, C.-F., ... Turunen, E. (2005). Diurnal variation of ozone depletion during the October–November 2003 solar proton events. *Journal of Geophysical Research: Space Physics*, *110*(A9). Retrieved from `http://dx.doi.org/10.1029/2004JA010932` doi: 10.1029/2004JA010932

Woodger, L. A., Halford, A. J., Millan, R. M., McCarthy, M. P., Smith, D. M., Bowers, G. S., ... Liang, X. (2015). A summary of the BARREL campaigns: Technique for studying electron precipitation. *Journal of Geophysical Research: Space Physics*, *120*(6), 4922–4935. Retrieved from `http://dx.doi.org/10.1002/2014JA020874` doi: 10.1002/2014JA020874

Yando, K., Millan, R. M., Green, J. C., & Evans, D. S. (2011). A Monte Carlo simulation of the NOAA POES Medium Energy Proton and Electron Detector instrument. *Journal of Geophysical Research: Space Physics*, *116*(A10). Retrieved from `http://dx.doi.org/10.1029/2011JA016671` doi: 10.1029/2011JA016671

Figure 1.

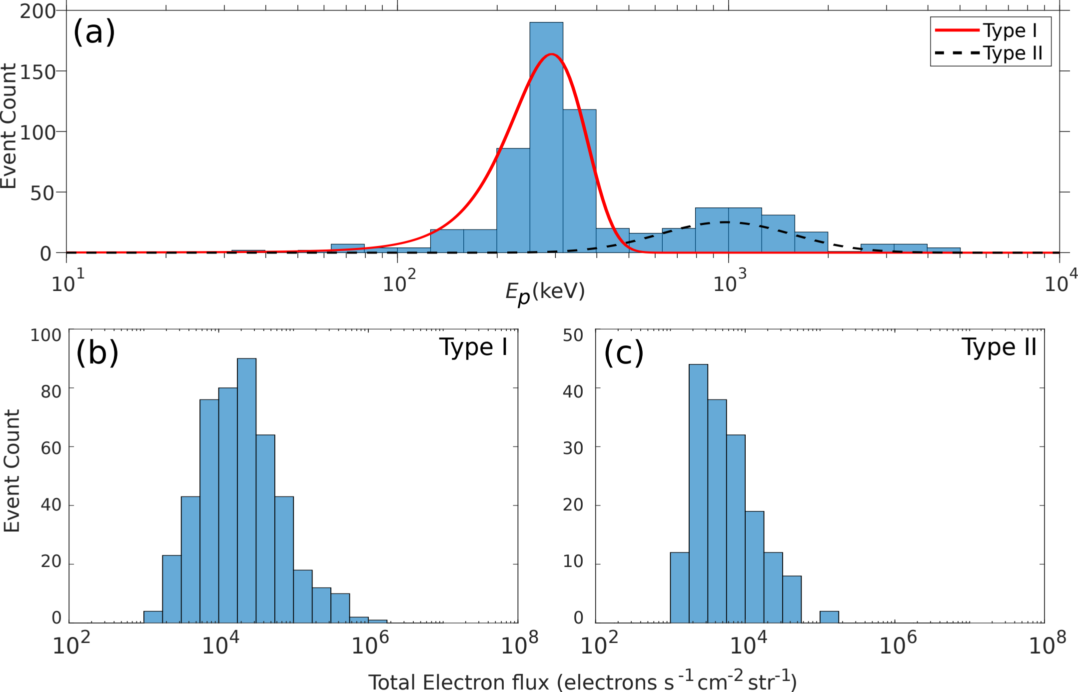

(a)
Type I
Type II
Event Count
200
150
100
50
0
10^1
10^2
10^3
10^4
E_p(keV)
(b)
Type I
(c)
Type II
Event Count
100
80
60
40
20
0
50
40
30
20
10
0
10^2
10^4
10^6
10^8
Total Electron flux (electrons s^{-1} cm^{-2} str^{-1})

Figure 2.

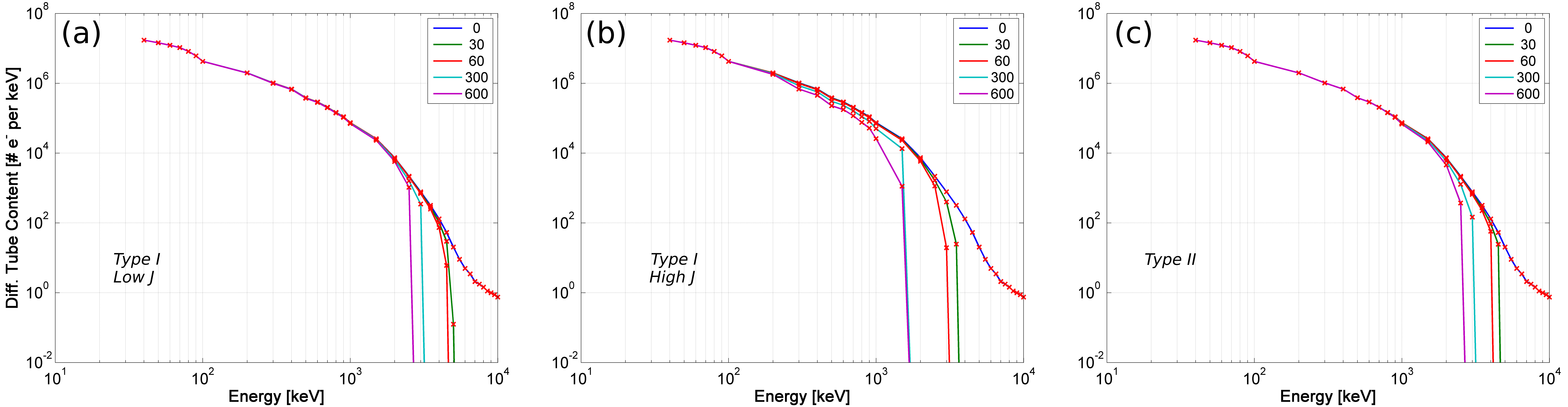

(a)
Type I
Low J
(b)
Type I
High J
(c)
Type II
0
30
60
300
600
Diff. Tube Content [# e⁻ per keV]
Energy [keV]

Figure 3.

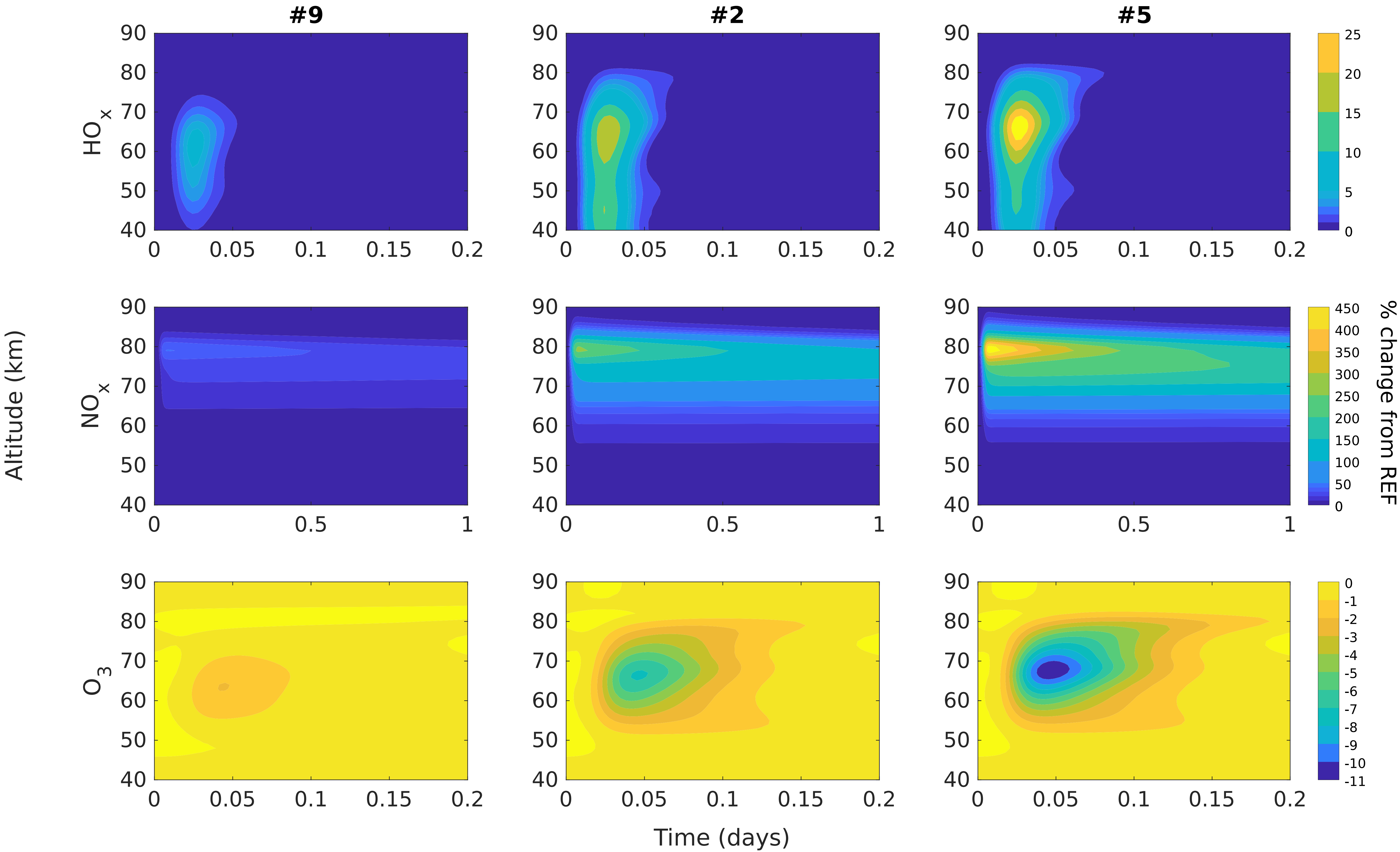
#9
#2
#5
HO_x
NO_x
O_3
Altitude (km)
Time (days)
% change from REF
90
80
70
60
50
40
0
0.05
0.1
0.15
0.2
0.5
1
25
20
15
10
5
450
400
350
300
250
200
150
100
-1
-2
-3
-4
-5
-6
-7
-8
-9
-10
-11

Figure 4.

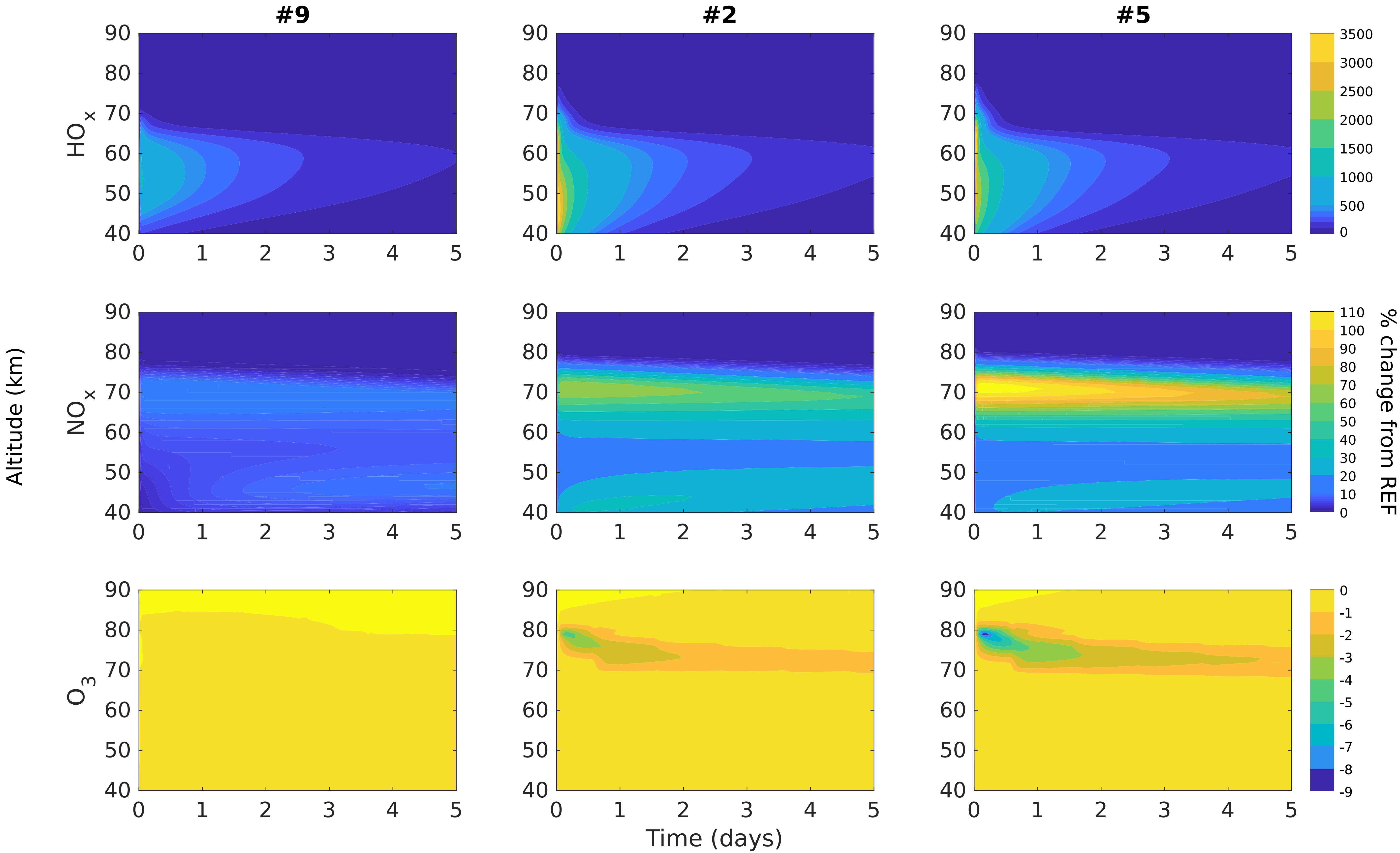

#9
#2
#5
HOx
NOx
O3
Altitude (km)
Time (days)
% change from REF
3500
3000
2500
2000
1500
1000
500
0
110
100
90
80
70
60
50
40
30
20
10
0
-1
-2
-3
-4
-5
-6
-7
-8
-9